ISSN 1063-7761, Journal of Experimental and Theoretical Physics, 2016, Vol. 123, No. 2, pp. 265–276. © Pleiades Publishing, Inc., 2016.
Original Russian Text © R.M. Khusnutdinoff, A.V. Mokshin, B.A. Klumov, R.E. Ryltsev, N.M. Chtchelkatchev, 2016, published in Zhurnal Eksperimental'noi i Teoreticheskoi Fiziki, 2016, Vol. 150, No. 2, pp. 306–319.

SOLIDS AND LIQUIDS

Structural Features and the Microscopic Dynamics of the Three-Component $Zr_{47}Cu_{46}Al_7$ System: Equilibrium Melt, Supercooled Melt, and Amorphous Alloy

R. M. Khusnutdinoff[a,b]*, A. V. Mokshin[a,b], B. A. Klumov[b,c,d], R. E. Ryltsev[b,e,f], and N. M. Chtchelkatchev[b,g,h]**

[a] *Kazan Federal University, Kazan, 420008 Russia*
[b] *Landau Institute for Theoretical Physics, Russian Academy of Sciences, Chernogolovka, Moscow oblast, 142432 Russia*
[c] *Aix-Marseille-Université, CNRS, Laboratoire PIIM, UMR 7345 13397, Marseille Cedex 20, France*
[d] *Joint Institute for High Temperatures, Russian Academy of Sciences, ul. Izhorskaya 13/19, Moscow, 125412 Russia*
[e] *Institute of Metallurgy, Ural Branch, Russian Academy of Sciences, ul. Amundsena 101, Yekaterinburg, 620016 Russia*
[f] *El'tsin Ural Federal University, ul. Mira 19, Yekaterinburg, 620002 Russia*
[g] *Moscow Institute of Physics and Technology, Institutskii per. 9, Dolgoprudnyi, Moscow oblast, 141700 Russia*
[h] *Institute of High-Pressure Physics, Russian Academy of Sciences, Troitsk, Moscow oblast, 142190 Russia*
**e-mail: khrm@mail.ru*
***e-mail: anatolii.mokshin@mail.ru*

Received January 22, 2016

Abstract—The structural and dynamic properties of the three-component $Zr_{47}Cu_{46}Al_7$ system are subjected to a molecular dynamics simulation in the temperature range $T = 250–3000$ K at a pressure $p = 1.0$ bar. The temperature dependences of the Wendt–Abraham parameter and the translation order parameter are used to determine the glass transition temperature in the $Zr_{47}Cu_{46}Al_7$ system, which is found to be $T_c \approx 750$ K. It is found that the bulk amorphous $Zr_{47}Cu_{46}Al_7$ alloy contains localized regions with an ordered atomic structures. Cluster analysis of configuration simulation data reveals the existence of quasi-icosahedral clusters in amorphous metallic Zr–Cu–Al alloys. The spectral densities of time radial distribution functions of the longitudinal ($\tilde{C}_L(k, \omega)$) and transverse ($\tilde{C}_T(k, \omega)$) fluxes are calculated in a wide wavenumber range in order to study the mechanisms of formation of atomic collective excitations in the $Zr_{47}Cu_{46}Al_7$ system. It was found that a linear combination of three Gaussian functions is sufficient to reproduce the $\tilde{C}_L(k, \omega)$ spectra, whereas at least four Gaussian contributions are necessary to exactly describe the $\tilde{C}_T(k, \omega)$ spectra of the supercooled melt and the amorphous metallic alloy. It is shown that the collective atomic excitations in the equilibrium melt at $T = 3000$ K and in the amorphous metallic alloy at $T = 250$ K are characterized by two dispersion acoustic-like branches related with longitudinal and transverse polarizations.

DOI: 10.1134/S1063776116060042

1. INTRODUCTION

Amorphous metallic alloys represent a new class of structural and functional materials with extraordinary properties, which differ from the properties of their crystalline analogs [1–3]. For example, amorphous metallic alloys have a high strength and elasticity and good plasticity during strong deformation [4, 5]. On the whole, this class of materials is characterized by a wide spectrum of unique physicochemical and mechanical properties, which attracts deep interest from a standpoint of both fundamental investigations and technological applications [4–6]. As a rule, amorphous metallic alloys are multicomponent systems having a high glass-forming ability, and their disordered phase can be formed by cooling of an equilibrium melt at a cooling rate $\gamma = 10^4–10^7$ K/s [7, 8]. The empirical rules that can be used to determine the melts that can form bulk metallic glasses were formulated for the first time in [1]. The authors of [9] showed that binary Cu–Zr melts have the highest glass-forming ability as compared to other binary metallic systems. Moreover, it was found that the glass-forming ability of binary Cu–Zr melts was significantly improved upon addition of a low aluminum content (usually less than 10 at % [10, 11]) and that the addition of 5–7 at % Al significantly increased the plasticity of an amorphous metallic Cu–Zr alloy [12]. Note that the Cu–

Zr–Al system is now represents the base of many bulk metallic glasses with interesting physical and mechanical properties [13].

It is assumed that, in contrast to equilibrium melts, the structure of metallic glasses is characterized by short- and medium-range orders caused by the existence of so-called quasi-icosahedral clusters [14, 15], which was experimentally supported recently [16]. According to Frank's hypothesis [17], icosahedra in a multiparticle system stabilize an amorphous phase and prevent its crystallization. To reveal the presence of icosahedral clusters in amorphous metallic alloys, researchers performed numerous experimental and molecular dynamics studies of the structural features of the $Zr_{46}Cu_{46}Al_8$, $Zr_{48}Cu_{45}Al_7$, $Zr_{45}Cu_{50}Al_5$, and $Zr_xCu_{90-x}Al_{10}$ systems [18–24]. The formation of a microstructure and its influence on the mechanical properties of an amorphous metallic $Zr_xCu_{90-x}Al_{10}$ alloy was considered in [25]. The authors of [26] studied the effect of alloying with aluminum atoms on the structure and the glass-forming ability of Zr–Cu melts. The electronic properties of amorphous metallic Zr–Cu–Al alloys were comprehensively analyzed in [27]. However, despite a large number of experimental and theoretical investigations, the mechanisms of formation of structural heterogeneities and their influence on the dynamic properties of metallic glasses are still poorly understood.

The purpose of this work is to simulate the atomic dynamics of the $Zr_{47}Cu_{46}Al_7$ system in a wide temperature range in order to study the changes in the atomic structure and dynamics caused by the amorphization of the three-component metallic melt.

2. SIMULATION PROCEDURE

The atomic dynamics simulation of the $Zr_{47}Cu_{46}Al_7$ system was carried out in the temperature range T = 250–3000 K at an external pressure p = 1.0 bar. This temperature range for this system covers the equilibrium liquid phase and the phases that correspond to a supercooled melt and an amorphous alloy. The system under study consisted of N = 32 000 atoms arranged in the cubic cell with periodic boundary conditions. The interatomic interaction was performed using the embedded-atom method (EAM) potential[1] [18], where the potential energy of the ith is expressed as [28]

$$U_i = F_\alpha\left(\sum_{j\neq i}\rho_\beta(r_{ij})\right) + \frac{1}{2}\sum_{j\neq i}\phi_{\alpha\beta}(r_{ij}). \quad (1)$$

Here, $\phi_{\alpha\beta}(r_{ij})$ is the short-range pair potential of the interatomic interaction, and $F(\rho)$ is the EAM potential, which takes into account multiparticle interactions in terms of the effective electron density ρ_i of the ith atom. Subscripts α and β designate the types of elements entering in the composition of the metallic melt, $\alpha, \beta \in$ {Zr, Cu, Al}. The equations of motion for atoms were integrated using the Verlet algorithm in the velocity form at a time step Δt = 1.0 fs [29].

A supercooled melt and an amorphous $Zr_{47}Cu_{46}Al_7$ alloy were prepared by rapid cooling of the equilibrium melt (at a temperature T = 3000 K) at a cooling rate $\gamma = 10^{12}$ K/s [30]. To bring the system to the state of thermodynamic equilibrium, we performed 5×10^5 time steps in an NpT ensemble and then 10^6 steps in an NVT ensemble to calculate the time and spectral characteristics.

3. SIMULATION RESULTS

3.1. Structural Features of the $Zr_{47}Cu_{46}Al_7$ System

3.1.1. Radial distribution functions. To analyze the structural features of the system, we calculated the partial components of the atomic radial distribution function (RDF) [31, 32]

$$g_{\alpha,\beta}(r) = \frac{L^3}{N_\alpha N_\beta}\left\langle\sum_{j=1}^{N_\alpha}\frac{n_{j\beta}(r)}{4\pi r^2\Delta r}\right\rangle, \quad (2)$$
$$\alpha,\beta \in \{\mathrm{Zr, Cu, Al}\}$$

for each temperature. Here, $n_{j\beta}(r)$ is the number of atoms of kind β within a spherical layer of thickness Δr at distance r from the jth atom; L is the edge length of the cell to be simulated; and N_α and N_β are the numbers of atoms of kind α and β, respectively.

Full RDF $g(r)$ is related to partial components $g_{\alpha,\beta}(r)$ as follows [33]:

$$g(r) = \sum_{\alpha=\beta} W_{\alpha,\beta}g_{\alpha,\beta}(r) + 2\sum_{\alpha\neq\beta} W_{\alpha,\beta}g_{\alpha,\beta}(r), \quad (3)$$

where $W_{\alpha,\beta} = c_a c_\beta f_\alpha f_\beta/(\sum c_i f_i)^2$ is the weight factor and c_i and f_i are the concentration and the atomic form factor of atoms of kind i, respectively [34].

Figure 1 shows the partial components of RDF $g_{\alpha,\beta}(r)$ at various temperatures T from the range 250–3000 K (the interval 250 K was taken for the temperature range $T \le 1500$ K, and the interval 500 K was used for the temperature range $T > 1500$ K). It is seen that, as the temperature decreases, the peaks in RDFs become more pronounced and the second peak in the $g_{\alpha,\beta}(r)$ curves is split. This splitting is usually related to the transition into a glass phase. Such features on the behavior of $g(r)$ are known to indicate the formation of local structures, which are characteristic of amorphous materials (see, e.g., [35]). Based on atomic dynamics simulation, the authors of [34] showed that $(Zr_{0.5}Cu_{0.5})_{100-x}Al_x$ melts have the best glass-forming ability at 7–8 at % Al.

[1] As was shown in [18], this potential model correctly reproduces the structural features and a number of thermomechanical characteristics of equilibrium and supercooled Zr–Cu–Al melts.

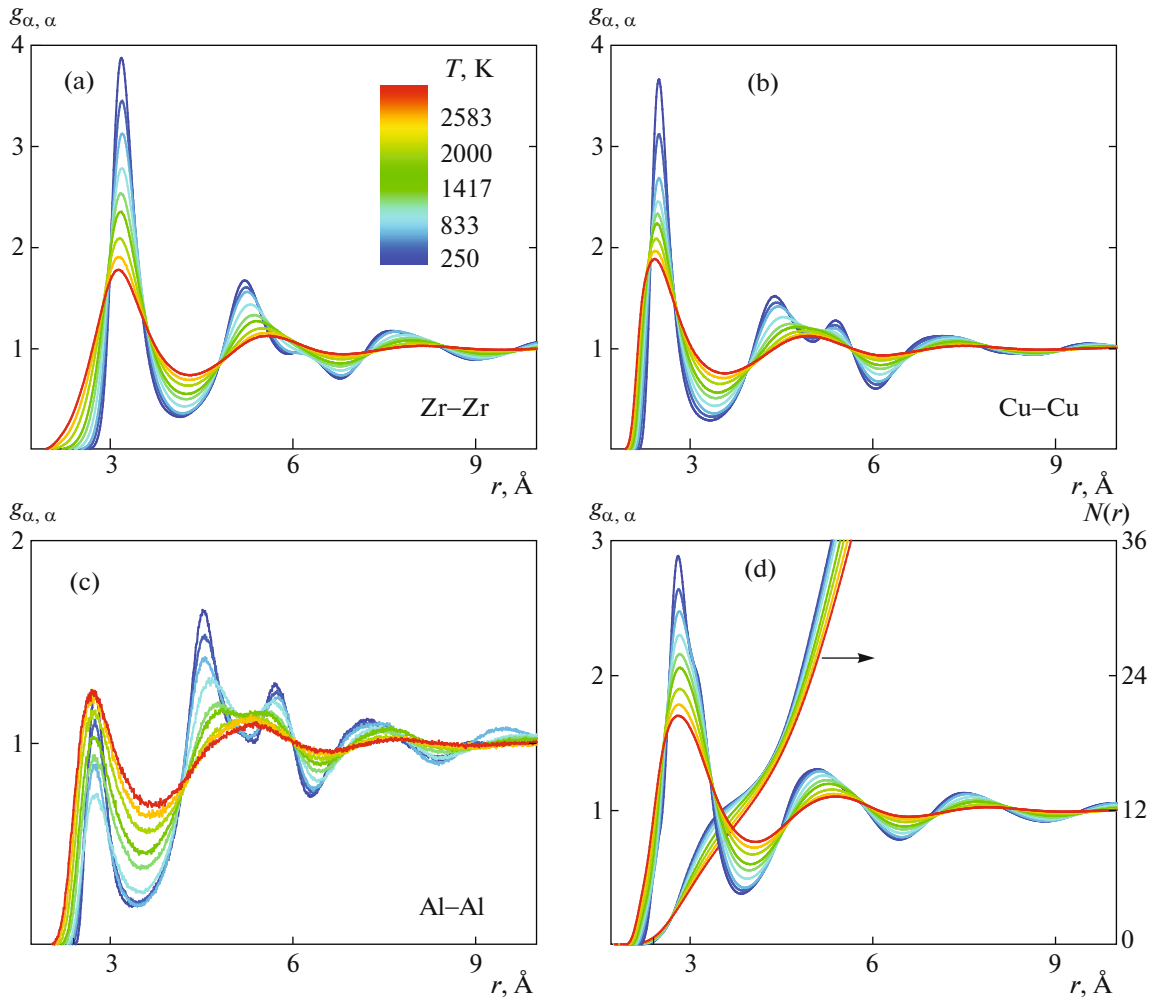

Fig. 1. (Color online) $Zr_{47}Cu_{46}Al_7$ system at various temperatures T: partial RDF components $g_{\alpha,\alpha}(r)$ for (a) Zr, (b) Cu, and (c) Al and full RDF $g(r)$. The color of the curve depends on temperature, which increases from blue to red. The splitting of the second peak in the $g_{\alpha,\alpha}(r)$, which is usually attributed to the transition into a glass phase, is detected at all partial distribution functions at low T. Shoulders, which characterize the formation of a chemical short-range order, appear near the first maximum in the full $g(r)$ function when T decreases. (d) Cumulative function $N(r) \equiv \int_0^r 4\pi x^2 g(x)dx$, which characterizes the number of particles in a sphere of radius r. At the temperatures under study, close atomic packing takes place, $N(r_m) \approx 12$ (r_m is the position of the first nonzero minimum in the $g(r)$ curve).

Note that shoulder-like structures appear in the full $g(r)$ function at T near the first maximum. These structures are likely to be associated with the formation of a chemical short-range order in the system under study (similar effect was observed in liquid gallium [36]). Figure 1d also shows the behavior of the cumulative function $N(r) \equiv \int_0^r 4\pi x^2 g(x)dx$, which gives the average number of particles in a sphere of radius r. It is clearly visible that close atomic packing takes place in this temperature range: 12 atoms are located in the first coordination shell. This important circumstance will be used to determine the properties of the orientational short-range order in the system under study.

3.1.2. Padé analysis of full RDF. As follows from definition (2), partial RDFs $g_{\alpha,\beta}(r)$ contain information on the atomic distribution in a multiparticle system: for example, the maxima in the first peak in $g_{\alpha,\beta}(r)$ curves correspond to the most probable distances between particles of kinds α and β within the first coordination shell (see Fig. 1). Unfortunately, no reliable method exists to measure $g_{\alpha,\beta}(r)$ experimentally and only full RDF $g(r)$ can be experimentally measured (see Eq. (3)). This function is usually determined from static structure factor $S(k)$, which is measured in experiments on neutron or X-ray diffraction [31].

Since function $g(r)$ is the superposition of $g_{\alpha,\beta}(r)$ functions (see Eq. (3)), information on the probable

Rotational invariants q_l and w_l (l = 4, 6) calculated for a number of crystal structures at a fixed number of nearest neighbors N_{nn}

Type of lattice	q_4	Q_6	w_4	W_6
HCP (N_{nn} = 12)	0.097	0.485	0.134	–0.012
FCC (N_{nn} = 12)	0.19	0.575	–0.159	–0.013
Icosahedral (N_{nn} = 12)	1.4×10^{-4}	0.663	–0.159	–0.169
BCC (N_{nn} = 8)	0.5	0.628	–0.159	0.013
BCC (N_{nn} = 14)	0.036	0.51	0.159	0.013

distance between two arbitrary particles of kinds α and β is averaged here. In [36], we proposed a method to process $g(r)$ using a numerical analytic continuation of RDF by a Padé approximation distribution. This method can be used to restore data on the distribution of particles in a multiparticle system.

Padé approximants can be used to interpolate and extrapolate a function set by a table of N points and, which is very important, to perform an analytic continuation into the complex plane of the argument of the function to be approximated. A Padé approximant is specified through a rational function determined as a ratio of two polynomials. On the other hand, a rational function is known to be represented by a continued fraction, which approximates a function much more accurately as compared to the representation of the function in the form of a series. To construct an approximant, we use the multipoint algorithm [37]. Let the values of function $f(x_i) = u_i$ be known at points x_i, where i = 1, 2, 3, ..., N. Then, Padé approximant $C_N(x)$ is constructed as follows:

$$C_N(x) = \cfrac{a_1}{\cfrac{a_2(x-x_1)}{\cfrac{a_3(x-x_2)}{\cfrac{a_4(x-x_3)}{\ldots a_N(x-x_{N-1})+1}+1}+1}+1}, \qquad (4)$$

where quantities a_i are determined from the condition $C_N(x_i) = u_i$, which is met if a_i satisfies the relations

$$a_i = g_i(x_i), \quad g_1(x_i) = u_i, \quad i = 1,2,3,\ldots,N, \qquad (5)$$

$$g_p(x) = \frac{g_{p-1}(x_{p-1}) - g_{p-1}(x)}{(x - x_{p-1})g_{p-1}(x)}, \quad p \geq 2. \qquad (6)$$

Equation (5) plays the role of a boundary condition for recursive Eq. (6). For example, for $x = x_{i_0}$, we find $g_1(x_{i_0})$ from Eq. (5) and $g_j(x_{i_0})$, j = 2, 3, ..., i, from Eq. (6).

Thus, we performed an analytic continuation of the $g(r)$ RDF calculated from simulation data into the complex plane of r using a Padé approximant. As an example, Fig. 2 shows an analytic continuation of $g(r)$ for the system at a temperature T = 250 K. As will be shown below, the real and imaginary parts of the pole coordinates contain information on the characteristic correlation lengths in a multiparticle system.

The static structure factor is related to $g(r)$ as [2]

$$S(k) = 1 + \frac{4\pi}{\rho}\mathrm{Im}\int_0^\infty r(g(r)-1)e^{ikr}dr, \qquad (7)$$

where k is the wavenumber. Thus, if function $g(r)$ has a pole at point r_p, this pole gives an oscillating contribution of the type $\cos(k\mathrm{Re}r_p)$ or $\sin(k\mathrm{Re}r_p)$ to the structure factor. The oscillation amplitude decreases with increasing wavevector k as $\exp(-k\mathrm{Im}r_p)$. Therefore, the poles of function $g(r)$ determine the characteristic spatial scales of the system of interacting particles. $g(r)$ turned out to be well approximated by a rational function with several poles. A Padé approximant can also be used to show that structure factor $S(k)$ has nonanalytical behavior (contains cuts) in the complex plane of k. This is associated with contributions of the type $\exp(-k\mathrm{Im}r_p)$ to $S(k)$.

The simulation data have a certain accuracy. Nevertheless, it can be shown that the numerical analytic continuation is stable despite the limited data accuracy.

In this work, the stability of the analytic continuation was tested by random sampling. 5% of the data were randomly removed from a table of the values of $g(r)$ and the remaining data were randomly permuted.

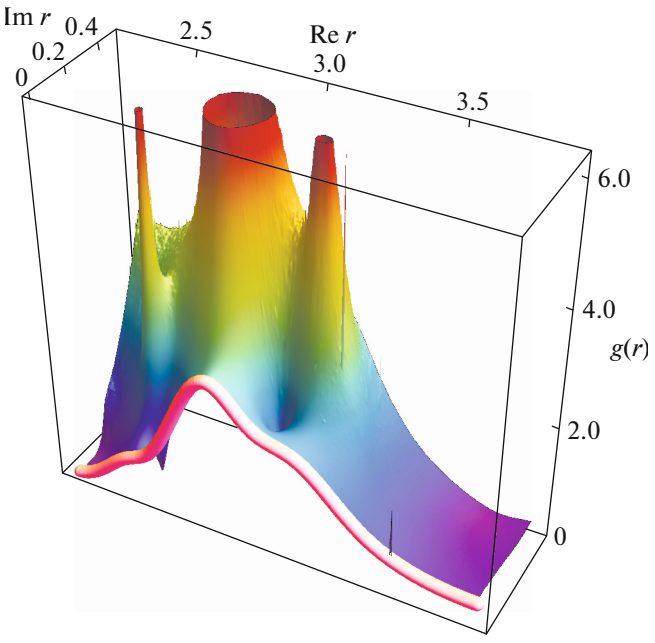

Fig. 2. (Color online) Analytic continuation of RDF $g(r)$ into the complex plane of t at T = 250 K (three-dimensional surface). (pink heavy curve) Full $g(r)$ function at real r and (peaks) poles of function $g(r)$ in the complex plane of r.

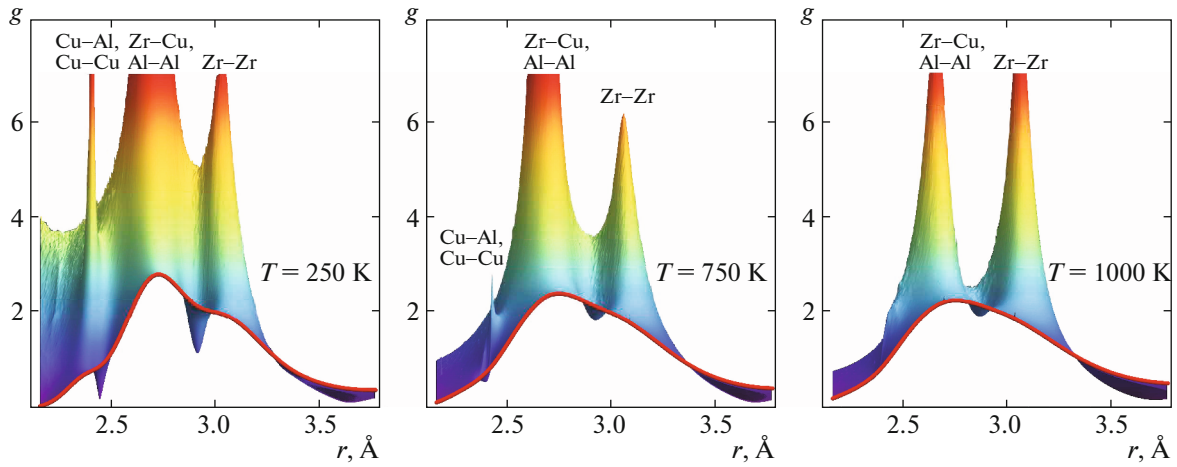

Fig. 3. (Color online) Padé analysis of RDF. (red curves) Full $g(r)$ function at real r. Each plot is a three-dimensional picture (which is similar to that in Fig. 2) for a certain temperature (axis Imr is normal to the picture plane). The peaks correspond to the poles of the $g(r)$ function in the complex plane of r. The $g(r)$ plots thus constructed make it possible to unambiguously reveal the correlation between the real part of the pole positions and the behavior of $g(r)$ at real r.

A Padé approximant was then constructed using a continued fraction [36, 38]. An analytic continuation of function $g(r)$ was constructed as a result of 100000 iterations. Figure 3 shows $g(r)$ RDF in the complex plane. The insufficient accuracy of the numerical calculations of function $g(r)$ manifests itself in the fact that a random sample can shift the pole positions. If a pole is stable, this shift is insignificant and a sharp peak rather than a singularity is observed in a picture after averaging. The position of the peak maximum in the complex plane is taken to be the coordinate of the pole. The real parts of the pole positions turned out to correspond to the most probable distances between particles of kinds α and β at a high accuracy (see Fig. 3). A structural crossover takes place at a temperature of about 750 K: the pole corresponding to Cu–Cu and Cu–Al correlations disappears. As will be shown below, this crossover also manifests itself in the temperature dependences of other quantities.

3.1.3. Wendt–Abraham parameters: temperature crossover. The melt–glass transition temperature was determined using the Wendt–Abraham parameter [39–41]

$$r^{WA}_{\alpha,\beta} = g^{(\min)}_{\alpha,\beta}/g^{(\max)}_{\alpha,\beta} \tag{8}$$

and the translation order parameter [42, 43]

$$t_{\alpha,\beta} = \frac{1}{r_{\max}}\int_0^{r_{\max}} |g_{\alpha,\beta}(r) - 1|dr, \quad \alpha,\beta \in \{\mathrm{Zr},\mathrm{Cu},\mathrm{Al}\}. \tag{9}$$

Here, $g^{(\max)}_{\alpha,\beta}$ and $g^{(\min)}_{\alpha,\beta}$ are the first maximum and the first nonzero minimum in $g(r)$ RDF. Note that the authors of [39] used this parameter as an indicator of the crystal–liquid transition in the Lennard-Jones system, and this indicator is now widely applied to determine the phase states and structural transitions in various systems (see, e.g., [44–47]).

Figure 4 shows the temperature dependences of the Wendt–Abraham parameter for the Zr–Zr, Cu–Cu, and Al–Al atomic pairs. From the intersections of the Wendt–Abraham parameter interpolation lines, we determined the critical glass transition temperature of the $Zr_{47}Cu_{46}Al_7$ system ($T_c \approx 750$ K). Note that this temperature agrees well with the simulation data for the $Zr_{45}Cu_{50}Al_5$ system ($T_c = 757.1$ K) [21]. The inset to Fig. 4 shows the temperature T dependences of the partial components of translation order parameter $t_{\alpha,\beta}$. It is seen that, as the temperature dependence of the Wendt–Abraham parameter $r^{WA}_{\alpha,\beta}(T)$, the temperature dependence of parameter $t_{\alpha,\beta}(T)$ in the semilogarithmic coordinates has two linear segments with an intersection point at $T \approx 750$ K. In addition, note that parameter $t_{\alpha,\beta}$ increases with decreasing temperature, which can be caused by the existence of local ordered regions in the system [48].

3.2. Orientational Short-Range Order in the $Zr_{47}Cu_{46}Al_7$ System

3.2.1. Bond order distribution function. To analyze the orientational short-range order in the $Zr_{47}Cu_{46}Al_7$ system, we first consider the behavior of the bond order distribution function (BADF) [49, 50]

$$P(\theta) = \frac{1}{Nn_\theta}\left\langle \sum_{k=1}^{N}\sum_{i=1}^{n_c}\sum_{j\neq i}^{n_c-1}\delta(\theta - \theta_{ikj})\right\rangle, \tag{10}$$

where n_θ is the number of the angles in the system that are formed by an arbitrary kth atom and its (any) two

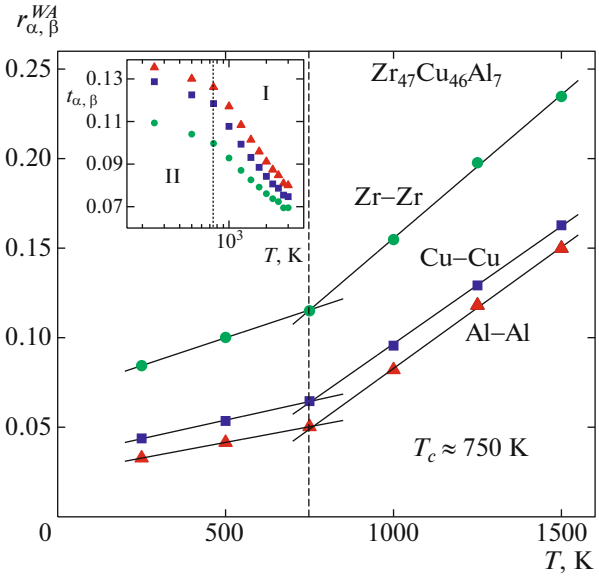

Fig. 4. (Color online) Temperature dependences of the Wendt–Abraham parameter calculated for the $Zr_{47}Cu_{46}Al_7$ system. (inset) Temperature dependence of the translation order parameter: (I) liquid and (II) supercooled liquid.

neighboring atoms and n_c is the number of all neighboring atoms for the kth atom. The neighboring atoms are taken to be the atoms that form the first coordination shell. n_c was determined from the condition of minimum in the partial components of RDF $g_{\alpha,\alpha}(r)$, where $\alpha \in \{Zr, Cu\}$. Figure 5 shows BADFs $P(\theta)$ for zirconium and copper atoms and for the full system in the temperature range under study.[2] Note that these pair angular distributions suggest the presence of hcp-like and icosahedral (ico-like) crystals at low temperatures. The existence of ordered clusters in the system can be determined much more exactly using rotational invariants to be discussed below.

As is seen from Fig. 5, the shape of BADF $P(\theta)$ changes significantly when temperature decreases: the peaks in the $P(\theta)$ function become more pronounced during the amorphization of the system, and an additional peak appears in the distribution at $\theta \approx 150°$. When studying a binary amorphous $Cu_{64}Zr_{36}$ alloy, the authors of [51] detected similar features in angular distribution $P(\theta)$ and explained them by the existence of regions with quasi-icosahedral symmetry. Note that the $P(\theta)$ function for the $Zr_{47}Cu_{46}Al_7$ melt almost coincides with the $P(\theta)$ function for the Lennard-Jones system, which is likely to indicate that this distribution is quasi-universal for other melts.

3.2.2. Behavior of rotational invariants. It is convenient to apply the rotational invariant method proposed in [52, 53] and widely used in the condensed-

[2]BADF $P(\theta)$ for aluminum atoms is not shown because of the high signal-to-noise ratio of aluminum.

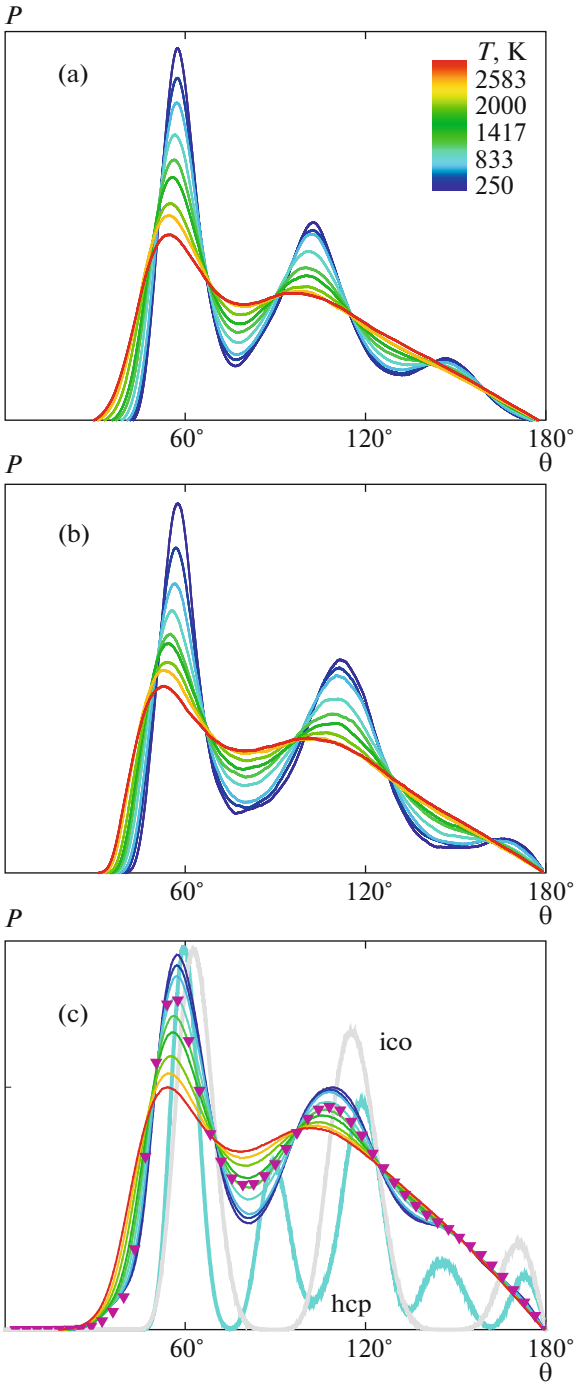

Fig. 5. (Color online) $Zr_{47}Cu_{46}Al_7$ system at various temperatures T from the range 250 K $\le T \le$ 3000 K (T step is 250 K at $T \le$ 1500 K, T step is 500 K at $T \ge$ 1500 K). Temperature dependences of $P(\theta)$ BADFs for (a) zirconium atoms, (b) copper atoms, and (c) full system. (c) For comparison, $P(\theta)$ distributions are presented for (triangles) Lennard-Jones melt, which are almost constant along the melting curve of the Lennard-Jones system and are a quasi-universal indication of a melt; (hcp, blue curve) hcp crystal lattice; and (ico, gray curve) icosahedral phase. Thermal atomic motion was taken into account in the two last cases.

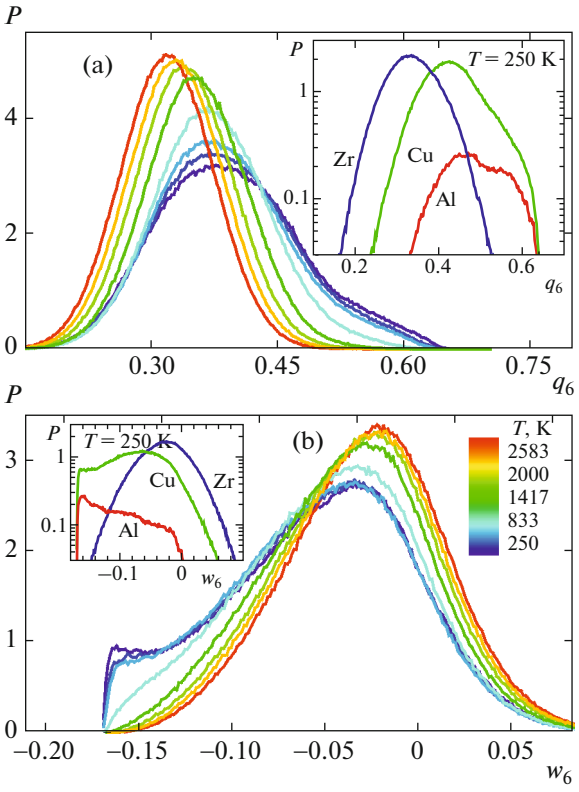

Fig. 6. (Color online) Orientational short-range order in the $Zr_{47}Cu_{46}Al_7$ system. Distributions of all atoms (a) $P(q_6)$ and (b) $P(w_6)$ over their rotational invariants q_6 and w_6, respectively, are presented for a number of temperatures. (inset) Partial $P(q_6)$ distributions for each atom ((red line) Al, (blue curve) Zr, and (green curve) Cu) for the glass phase at $T = 250$ K. It is seen that icosahedral clusters form only on the basis of zirconium and aluminum and copper is retained in the disordered phase.

matter physics [54–64] in order to determine the parameters that characterize a short-range order and contain angular correlations with a higher order than BADF $P(\theta)$.

In terms of this approach, the number of nearest neighbors $N_b(i)$ is first determined for every ith particle. Vectors $\mathbf{r}_{ij}$ connecting particle i to the nearest neighbors ($j = 1, N_b$) can be used to determine bond order parameter $q_{lm}(i)$ for every atom/particle,

$$q_{lm}(i) = \frac{1}{N_b(i)} \sum_{j=1}^{N_b(i)} Y_{lm}(\theta_j, \phi_j), \qquad (11)$$

where $Y_{lm}(\theta, \phi)$ are spherical harmonics and θ and ϕ are the angular coordinates of the jth particle that are determined by vector $\mathbf{r}_{ij}$. Note that the local short-range order thus determined depends only on two parameters, namely, angular nearest-neighbor distributions θ_i and ϕ_i. Here, the neighbors are considered to be all particles in the first coordination shell. Using parameter $q_{lm}(i)$, we calculate the rotational invariants of second ($q_l(i)$) and third ($w_l(i)$) kind for every particle,

$$q_l(i) = \left(\frac{4\pi}{2l+1} \sum_{m=-l}^{m=l} |q_{lm}(i)|^2 \right)^{1/2}, \qquad (12)$$

$$w_l(i) = \sum_{\substack{m_1,m_2,m_3 \\ m_1+m_2+m_3=0}} \begin{pmatrix} l & l & l \\ m_1 & m_2 & m_3 \end{pmatrix} q_{lm_1}(i) q_{lm_2}(i) q_{lm_3}(i), \qquad (13)$$

where $\begin{pmatrix} l & l & l \\ m_1 & m_2 & m_3 \end{pmatrix}$ are the Wigner $3j$ symbols. The sum in the latter equation is taken over all indices $m_i = -l, \ldots, l$ that meet the condition $m_1 + m_2 + m_3 = 0$.

It is important that each type of crystal lattice has a unique set of rotational invariants q_l and w_l. This specific feature makes it possible to determine an ordered structure detected experimentally or simulated by comparing q_l and w_l calculated for every particle with q_l^{id} and w_l^{id} for ideal lattices. To identify a crystal structure, researchers usually apply rotational invariants of the second (q_4, q_6) and third (w_4, w_6) kinds, which can easily be calculated for ideal crystals. These invariants are given in the table for various lattices.

Figure 6 shows distributions $P(q_6)$ and $P(w_6)$ over rotational invariants $q_6(i)$ and $w_6(i)$ at various temperatures. It is clearly visible that a decrease in the temperature leads to the appearance of particles with $q_6 > 0.6$ and $w_6 < -0.15$ in the system, which is characteristic of icosahedral symmetry (also see table). The ideal icosahedron has $q_6^{ico} \approx 0.66$ and $w_6^{ico} \approx -0.17$, so that the detected icosahedra are strongly distorted (but retaining five-ray structure). Note that the authors of [16] experimentally studied a metallic $Zr_{80}Pt_{20}$ glass and observed distorted icosahedral clusters with similar values of rotational invariants. The appearance of such clusters in the system under study is more obvious when two-dimensional atom distributions are plotted on the q_4–q_6 pane for various temperatures (Fig. 7). It is seen that atoms in the liquid phase (at high temperatures $T \geq 2000$ K) are disordered. As the temperature decreases, hcp-like clusters based on zirconium and aluminum atoms first form, and a distorted icosahedral (ico-like) phase with zirconium and aluminum atoms located in the base of icosahedral clusters then forms. It is interesting that copper atoms are disordered at all temperatures. Note that similar structural behavior upon cooling the melt is also observed in the absence of aluminum, for the binary Cu–Zr system.

It should be noted that atomic groups with icosahedral symmetry exist in the case of the supercooled melt and the amorphous alloy and that such local ordered groups are absent in the case of the equilibrium melt. As a rule, the appearing ordered atomic groups are

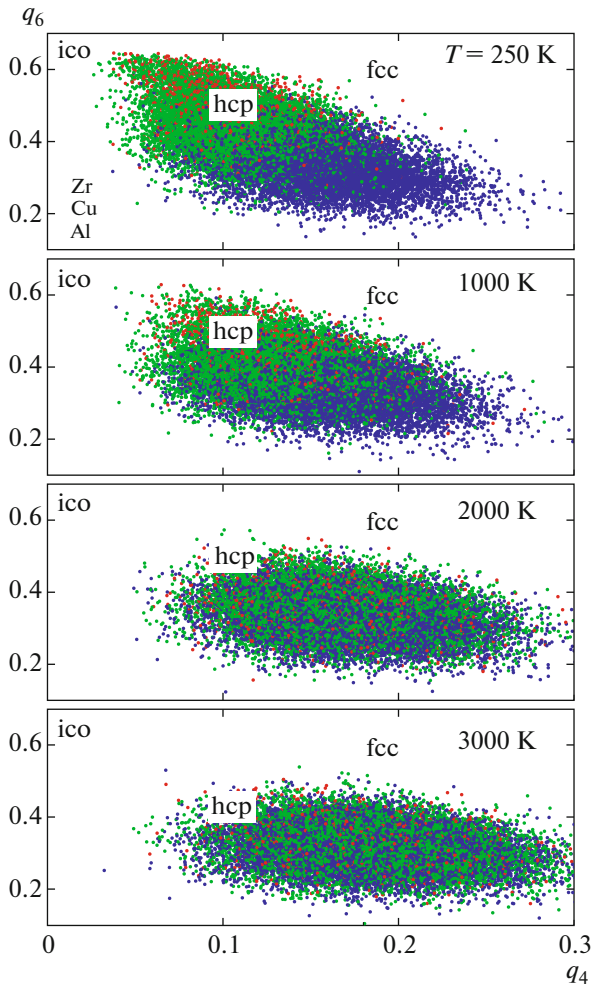

Fig. 7. (Color online) Orientational short-range order in the $Zr_{47}Cu_{46}Al_7$ system at various temperatures. The distributions of (green line) zirconium, (blue) copper, and (red) aluminum atoms in the plane of rotational invariants q_4–q_6 calculated for a fixed number of nearest neighbors for each particle ($N_{nn} = 12$). The positions of ico, hcp, and fcc rectangles correspond to ideal crystals with icosahedral, hcp, and fcc symmetry, respectively.

represented by incomplete icosahedra and small fragments of icosahedra uniformly distributed over the entire system. Figure 8 shows the atoms that form the amorphous $Zr_{47}Cu_{46}Al_7$ alloy at $T = 250$ K and are involved in structural aggregates with pronounced icosahedral symmetry. The structure shown as an example in Fig. 8 consists of 1894 atoms and the fractions of Zr, Cu, and Al atoms are 49, 43, and 8 at %, respectively.

3.3. Microscopic Dynamics of the $Zr_{47}Cu_{46}Al_7$ System

Information on collective atomic dynamics is in the spectral densities [65–67]

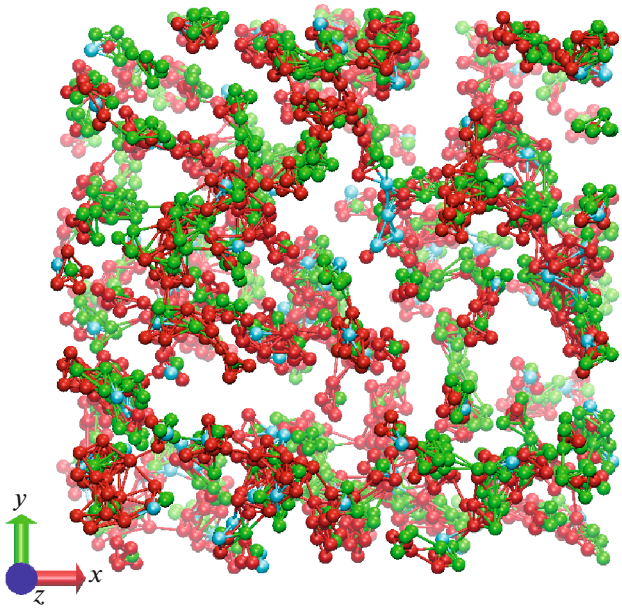

Fig. 8. (Color online) Result of cluster analysis, as applied to the data of simulating the atomic dynamics of the amorphous $Zr_{47}Cu_{46}Al_7$ alloy at $T = 250$ K. The atoms entering into a quasi-icosahedral structure are presented. (red balls) Zr atoms (49 at %), (green balls) Cu atoms (43 at %), and (blue balls) Al atoms (8 at %).

$$\tilde{C}_\alpha(k,\omega) = \frac{k_B T}{\pi m}\int_0^\infty C_\alpha(k,t)e^{-i\omega t}dt, \quad \alpha \in \{L,T\}, \tag{14}$$

of the normalized time correlation functions of the longitudinal,

$$C_L(k,t) = \frac{\langle(\mathbf{e}_k \cdot \mathbf{j}^*(k,0))(\mathbf{e}_k \cdot \mathbf{j}(k,t))\rangle}{\langle|\mathbf{e}_k \cdot \mathbf{j}(k,0)|^2\rangle} \tag{15}$$

and the transverse,

$$C_T(k,t) = \frac{\langle[\mathbf{e}_k \times \mathbf{j}^*(k,0)][\mathbf{e}_k \times \mathbf{j}(k,t)]\rangle}{\langle|\mathbf{e}_k \cdot \mathbf{j}(k,0)|^2\rangle} \tag{16}$$

fluxes [68, 69]. Here, the angle parentheses mean averaging over an ensemble of particles, and $\mathbf{j}(k, t)$ is the microscopic flux

$$\mathbf{j}(k,t) = \frac{1}{\sqrt{N}}\sum_l^N \mathbf{v}_l(t)\exp[-i(\mathbf{k}\cdot\mathbf{r}_l(t))], \tag{17}$$

where $\mathbf{v}_l(t)$ is the velocity of the lth particle at time t and $\mathbf{e}_k = \mathbf{k}/|\mathbf{k}|$ is the unit vector along vector $\mathbf{k}$.

Figure 9 shows the calculated frequency spectra of the longitudinal and transverse fluxes for the equilibrium melt at $T = 3000$ K, the supercooled melt ($T =$ 1000 K), and the amorphous metallic $Zr_{47}Cu_{46}Al_7$ melt ($T = 250$ K) at a wavenumber $k = k_m/2 \approx 1.30$ Å^{-1}, which corresponds to the boundary of the first Brill-

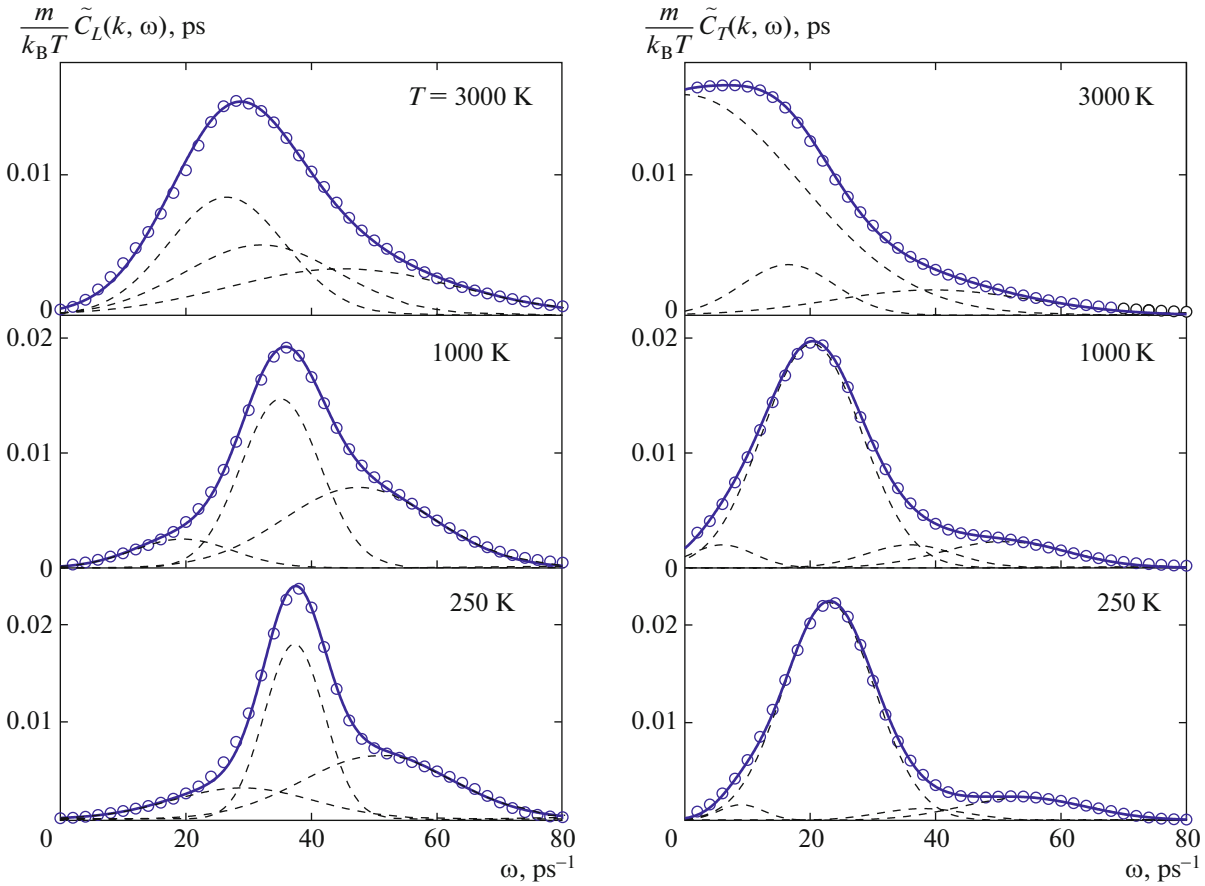

Fig. 9. (Color online) Spectral densities of the time correlation functions of the longitudinal ($\tilde{C}_L(k, \omega)$) and transverse ($\tilde{C}_T(k, \omega)$) fluxes for the equilibrium melt ($T = 3000$ K), the supercooled melt ($T = 1000$ K), and the amorphous metallic $Zr_{47}Cu_{46}Al_7$ alloy ($T = 250$ K) at $k \approx 1.30$ Å^{-1}: (points) atomic dynamics simulation, (solid curves) fitting with a linear combination of Gaussian functions, and (dashed curves) individual contributions (see Eq. (18)).

ouin pseudozone (k_m is the position of the principal maximum in static structure factor $S(k)$), in comparison with the results of fitting with a linear combination of Gaussian functions,

$$\tilde{C}_\alpha(k,\omega) = \frac{k_B T}{m}\sum_i \mathcal{A}_i(k)\exp(-\mathcal{B}_i(k)[\omega-\omega_i(k)]^2), \quad (18)$$
$$\alpha \in \{L, T\}.$$

Here, $\mathcal{A}_i(k)$ are weight coefficients, $\mathcal{B}_i(k)$ are quadratic time scales, and frequencies $\omega_i(k)$ determine the positions of the peaks in the $\tilde{C}_\alpha(k, \omega)$ spectrum. It is seen from Fig. 9 that, as temperature decreases, the spectra are complicated and specific features appear at high frequencies $\omega \geq 50$ ps^{-1}. A linear combination of three Gaussian contributions is sufficient to take into account all specific features in the $\tilde{C}_L(k, \omega)$ spectra of the longitudinal flux for the equilibrium melt, the supercooled melt, and the amorphous alloy, whereas at least four Gaussian functions are necessary to describe the $\tilde{C}_T(k, \omega)$ spectra of the transverse flux for the supercooled melt and the amorphous alloy. The corresponding peaks in the spectral densities of the time correlation functions of the longitudinal and transverse fluxes point to the existence of propagating collective longitudinal- and transverse-polarization excitations in the $Zr_{47}Cu_{46}Al_7$ system. Using the maxima of the spectral densities of the time correlation functions of the longitudinal ($\tilde{C}_L(k, \omega)$) and transverse ($\tilde{C}_T(k, \omega)$) fluxes, we plotted dispersion curves for the longitudinal ($\omega_c^{(L)}(k)$) and transverse ($\omega_c^{(T)}(k)$) polarizations in the temperature range under study.

Figure 10 depicts the obtained dispersion laws $\omega_c^{(L)}(k)$ and $\omega_c^{(T)}(k)$ for the $Zr_{47}Cu_{46}Al_7$ system at temperatures $T = 3000$ and 250 K. The dispersion curve related to the transverse-polarization oscillation processes in the melt at $T = 3000$ K is found to have a "window" of width k_0^T, where $\omega_c^{(T)}(k)$ begins to grow from a nonzero value of wavevector k and a shift by k_0^T is detected along axis k. This window in the dispersion

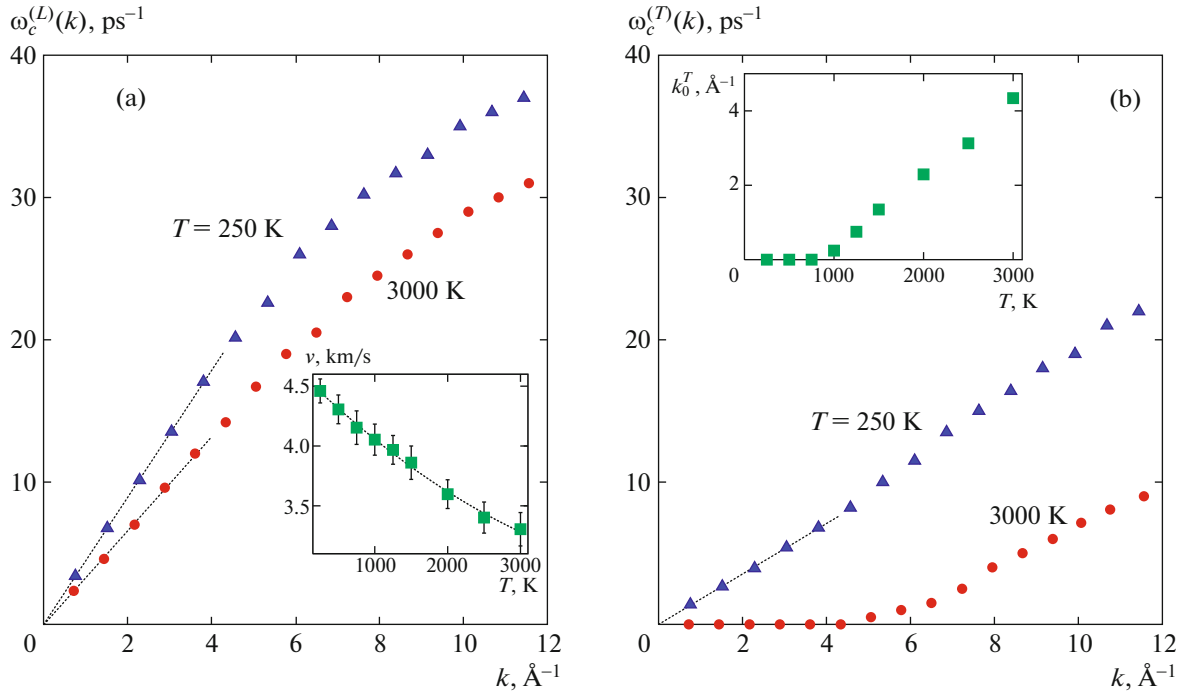

Fig. 10. (Color online) Dispersion curves of the collective excitations in the $Zr_{47}Cu_{46}Al_7$ system at temperatures of 250 and 3000 K for (a) longitudinal $\omega_c^{(L)}$ and (b) transverse $\omega_c^{(T)}$ polarization. Temperature dependences of (inset to (a)) sound velocity in the melt and (inset to (b)) gap width k_0^T in the transverse-polarization dispersion curve $\omega_c^{(T)}(k)$.

$\omega_c^{(T)}(k)$ curve is associated with the absence of macroelastic properties of the melt [65]. The temperature dependence of the window width ($k_0^T(T)$) in the dispersion curve of transverse polarization $\omega_c^{(T)}(k)$ is shown in the inset to Fig. 10b. It is seen that, as the temperature decreases, window width k_0^T in the $\omega_c^{(T)}(k)$ dispersion curve decreases and the window in the transverse-polarization dispersion curve disappears at a temperature below the critical glass transition temperature ($T_c \approx 750$ K), which is caused by the elastic properties of the amorphous metallic $Zr_{47}Cu_{46}Al_7$ alloy. The inset to Fig. 10a presents the values of sound velocity v obtained at several temperatures from the dispersion curves in the range of extremely low values of the wavevector. The temperature dependence of sound velocity in the medium ($v(T)$) is seen to grow monotonically when the equilibrium melt transforms into the supercooled liquid.

4. CONCLUSIONS

A large-scale simulation of the atomic dynamics of the $Zr_{47}Cu_{46}Al_7$ system was performed over a wide temperature range ($T = 250$–3000 K) at a pressure $p =$ 1.0 bar. When analyzing the calculated structural characteristics and the order parameters, we determined the critical glass transition temperature ($T_c \approx 750$ K). The supercooled $Zr_{47}Cu_{46}Al_7$ melt was found to have local ordered regions. Cluster analysis supports the hypothesis of existence of quasi-icosahedral clusters in amorphous metallic Zr–Cu–Al alloys. The calculated spectral densities of the time correlation functions of the longitudinal ($\tilde{C}_L(k, \omega)$) and transverse ($\tilde{C}_T(k, \omega)$) fluxes revealed propagating collective longitudinal- and transverse-polarization excitations in a wide wavenumber range for the equilibrium liquid, the supercooled melt, and the amorphous metallic alloy in the system under study. It was shown that a linear combination of three Gaussian functions is sufficient to reproduce the spectra of the longitudinal flux, whereas at least four Gaussian contributions are necessary to exactly reproduce the spectra of the transverse flux.

ACKNOWLEDGMENTS

We thank B.N. Galimzyanov for performing the calculations related to cluster analysis and preparing Fig. 8. The large-scale molecular dynamics calculations were carried out at the calculation cluster of Kazan Federal University and the supercomputer of the Interdepartmental Supercomputer Center of the Russian Academy of Sciences.

This work was supported in part by the Russian Science Foundation, project no. 14-12-01185.

REFERENCES

1. A. Inoue, Acta Mater. **48**, 279 (2000).
2. Y. Waseda, The Structure of Non-Crystalline Materials: Liquids and Amorphous Solids (McGraw-Hill, New York, 1980).
3. N. H. March, *Liquid Metals: Concepts and Theory* (Cambridge Univ. Press, Cambridge, 1990).
4. W. H. Wang, Adv. Mater. **21**, 4524 (2009).
5. C. Suryanarayana and A. Inoue, *Bulk Metallic Glasses* (CRC, Boca Raton, 2010).
6. R. M. Khusnutdinov, A. V. Mokshin, and I. I. Khadeev, J. Surf. Invest.: X-ray, Synchrotron Neutron Tech. **8**, 84 (2014).
7. N. Nishiyama and A. Inoue, Acta Mater. **47**, 1487 (1999).
8. R. M. Khusnutdinov and A. V. Mokshin, Bull. Russ. Acad. Sci.: Phys. **74**, 640 (2010).
9. W. F. Wu and Y. Li, Appl. Phys. Lett. **95**, 011906 (2009).
10. A. Inoue and W. Zhang, Mater. Trans. **43**, 2921 (2002).
11. Q. Wang, C. Dong, J. B. Qiang, and Y. M. Wang, Mater. Sci. Eng. A **449**, 18 (2007).
12. G. Kumar, T. Ohkubo, T. Mukai, and K. Hono, Scr. Mater. **57**, 173 (2007).
13. D. H. Xu, G. Duan, and W. L. Johnson, Phys. Rev. Lett. **92**, 245504 (2004).
14. D. B. Miracle, Nature Mater. **3**, 697 (2004).
15. H. W. Sheng, W. K. Luo, F. M. Alamgir, et al., Nature (London) **439**, 419 (2006).
16. A. Hirata, L. J. Kang, T. Fujita, et al., Science **341**, 376 (2013).
17. F. Frank, Proc. R. Soc. London, Math. Phys. Sci. **215**, 43 (1952).
18. Y. Q. Cheng, E. Ma, and H. W. Sheng, Phys. Rev. Lett. **102**, 245501 (2009).
19. L. Yang, G. Q. Guo, L. Y. Chen, et al., Scr. Mater. **63**, 879 (2010).
20. Ch. E. Lekka, J. Alloys Comp. **504**, S190 (2010).
21. Y. Zhang, N. Mattern, and J. Eckert, J. Appl. Phys. **110**, 093506 (2011).
22. J. Antonowicz, A. Pietnoczka, W. Zalewski, et al., J. Alloys Comp. **509**, S34 (2011).
23. C. C. Wang and C. H. Wong, J. Alloys Comp. 510, 107 (2012).
24. C. Tang and C. H. Wong, J. Non-Cryst. Sol. **422**, 39 (2015).
25. S. K. Deb Nath, J. Non-Cryst. Sol. **409**, 95 (2015).
26. C. Y. Yu, X. J. Liu, G. P. Zheng, et al., J. Alloys Comp. **627**, 48 (2015).
27. C. C. Yuan, X. Shen, J. Cui, et al., Appl. Phys. Lett. **101**, 021902 (2012).
28. D. K. Belashchenko, Phys. Usp. **56**, 1176 (2013).
29. M. P. Allen and D. J. Tildesley, *Computer Simulation of Liquids* (Clarendon, Oxford, 1987).
30. R. M. Khusnutdinoff, A. V. Mokshin, and I. D. Takhaviev, Phys. Solid State **57**, 412 (2015).
31. J. P. Hansen and I. R. McDonald, *Theory of Simple Liquids* (Academic, New York, 2006).
32. R. M. Khusnutdinoff and A. V. Mokshin, J. Non-Cryst. Sol. **357**, 1677 (2011).
33. A. V. Mokshin, A. V. Chvanova, and R. M. Khusnutdinoff, Theor. Math. Phys. **171**, 541 (2012).
34. Y. Zhang, N. Mattern, and J. Eckert, J. Alloys Comp. 514, 141 (2012).
35. G. N. Sarkisov, Phys. Usp. **45**, 597 (2002).
36. N. M. Chtchelkatchev, B. A. Klumov, R. E. Ryltsev, et al., arXiv:1512.00989.
37. H. Vidberg and J. Serene, J. Low Temp. Phys. **29**, 179 (1977).
38. N. M. Chtchelkatchev and R. E. Ryltsev, JETP Lett. **102**, 643 (2015).
39. H. J. Raveche, R. D. Mountain, and W. B. Streett, J. Chem. Phys. **61**, 1970 (1974).
40. H. R. Wendt and F. F. Abraham, Phys. Rev. Lett. **41**, 1244 (1978).
41. R. M. Khusnutdinoff, A. V. Mokshin, and R. M. Yul'met'ev, J. Exp. Theor. Phys. **108**, 417 (2009).
42. H. Tanaka, Phys. Rev. Lett. **80**, 5750 (1998).
43. A. V. Mokshin, R. M. Yul'met'ev, R. M. Khusnutdinoff, and P. Hanggi, J. Exp. Theor. Phys. **103**, 841 (2006).
44. S. A. Khrapak, B. A. Klumov, P. Huber, et al., Phys. Rev. Lett. **106**, 205001 (2011).
45. S. A. Khrapak, B. A. Klumov, P. Huber, et al., Phys. Rev. E **85**, 066407 (2012).
46. B. A. Klumov, JETP Lett. **98**, 259 (2013).
47. Yu. Fomin, V. N. Ryzhov, B. A. Klumov, and E. N. Tsiok, J. Chem. Phys. **141**, 034508 (2014).
48. R. E. Ryltsev and N. M. Chtchelkatchev, Phys. Rev. E **88**, 052101 (2013).
49. R. M. Khusnutdinoff, Colloid. J. **75**, 726 (2013).
50. U. Balucani and M. Zoppi, *Dynamics of the Liquid State* (Clarendon, Oxford, 1994).
51. J. Zemp, M. Celino, B. Schönfeld, and J. F. Löffler, Phys. Rev. B **90**, 144108 (2014).
52. P. J. Steinhardt, D. Nelson, and M. Ronchetti, Phys. Rev. Lett. **47**, 1297 (1981); P. J. Steinhardt, D. R. Nelson, and M. Ronchetti, Phys. Rev. B **28**, 784 (1983).
53. A. C. Mitus and A. Z. Patashinskii, Phys. Lett. A 87, 179 (1982), A. C. Mitus and A. Z. Patashinskii, Phys. Lett. A **88**, 31 (1983).
54. P. R. tenWolde, M. J. Ruiz-Montero, and D. Frenkel, J. Chem. Phys. **104**, 9932 (1996).
55. S. Torquato, T. M. Truskett, and P. G. Debenedetti, Phys. Rev. Lett. **84**, 2064 (2000).
56. U. Gasser, E. R. Weeks, A. Schofield, et al., Science **292**, 5515 (2001).
57. V. Luchnikov, A. Gervois, P. Richard, et al., J. Mol. Liq. **96**, 185 (2002).
58. J. R. Errington, P. G. Debenedetti, and T. Torquato, J. Chem. Phys. **118**, 2256 (2003).
59. A. V. Mokshin and J.-L. Barrat, Phys. Rev. E **77**, 021505 (2008).

60. A. V. Mokshin and J.-L. Barrat, J. Chem. Phys. **130**, 034502 (2009).
61. A. V. Mokshin, B. N. Galimzyanov, and J.-L. Barrat, Phys. Rev. E **87**, 062307 (2013).
62. B. A. Klumov, Phys. Usp. **53**, 1053 (2010).
63. T. Kawasaki and H. Tanaka, J. Phys.: Condens. Matter **22**, 232102 (2010).
64. B. A. Klumov, S. A. Khrapak, and G. E. Morfill, Phys. Rev. B **83**, 184105 (2011).
65. A. V. Mokshin, R. M. Khusnutdinoff, A. G. Novikov, N. M. Blagoveshchenskii, and A. V. Puchkov, J. Exp. Theor. Phys. **121**, 828 (2015).
66. R. M. Khusnutdinoff and A. V. Mokshin, Physica A **391**, 2842 (2012).
67. W. Montfrooij and I. de Schepper, Excitations in Simple Liquids, Liquid Metals and Superfluids (Oxford Univ. Press, New York, 2010).
68. R. M. Khusnutdinoff and A. V. Mokshin, JETP Lett. **100**, 39 (2014).
69. D. Pines, *Elementary Excitations in Solids* (Benjamin, New York, 1963).

Translated by K. Shakhlevich